Journal of Power Sources 210 (2012) 204–217

Contents lists available at SciVerse ScienceDirect

Journal of Power Sources

journal homepage: www.elsevier.com/locate/jpowsour

The influence of pore formers on the microstructure of plasma-sprayed NiO–YSZ anodes

Michael Poon[a], Olivera Kesler[b,*]

[a] Department of Mechanical Engineering, University of British Columbia, 2054-6250 Applied Science Lane, Vancouver, BC, Canada V6T 1Z4
[b] Department of Mechanical and Industrial Engineering, University of Toronto, 5 King's College Road, Toronto, ON, Canada M5S 3G8

ARTICLE INFO

Article history:
Received 2 November 2011
Received in revised form 13 February 2012
Accepted 15 February 2012
Available online 23 February 2012

Keywords:
SOFC
Plasma spray
Anode
Pore former

ABSTRACT

Four types of pore formers: high-density polyethylene (HDPE), polyether-ether-ketone (PEEK), mesocarbon-microbead (MCMB) carbon powder, and baking flour, are processed and characterized, then incorporated with NiO–YSZ nano-agglomerate powder to produce plasma sprayed SOFC anode coatings. Scanning electron microscopy (SEM) of the coating microstructure, gas permeability measurements, and porosity determinations by image analysis are used to evaluate the effectiveness of each potential pore former powder. Under the spray conditions studied, the flour and MCMB pore former powders are effective as plasma sprayed pore formers, increasing the permeability of the coatings by factors of four and two, respectively, compared to a similarly sprayed NiO–YSZ coating without pore formers. The HDPE powder is unable to survive the plasma spray process and does not contribute to the final coating porosity. The PEEK pore former, though ineffective with the current powder characteristics and spray parameters, exhibits the highest relative deposition efficiency and the most favorable thermal characteristics.

© 2012 Elsevier B.V. All rights reserved.

1. Introduction

Fuel cells are electrochemical devices that directly convert chemical energy to electrical energy with high efficiency and low environmental impact. Solid oxide fuel cells (SOFCs) are particularly attractive because of their capacity to use a variety of fuels, including gaseous hydrogen and hydrocarbons. However, to make SOFCs a more commercially attractive option, there is a need to lower production costs – by reducing the cost of raw materials, and/or by reducing the fabrication costs. The use of a plasma spray method for the production of SOFCs may provide a solution to both the material and fabrication costs, most notably by facilitating the fabrication of SOFCs on low-cost metallic supports.

Plasma spraying is a proven industrial process that can create ceramic coatings quickly and cost-effectively. However, a significant challenge for plasma sprayed SOFCs has been the ability to achieve the desired porosity of each layer. Plasma-sprayed coatings typically have porosities in the range of 5–15 vol.%; however, the different layers of an SOFC require porosities well above or well below this typical range. The electrolyte layer of an SOFC must be gas-tight, requiring highly dense ceramic coatings with no cracks and near-zero open porosity. On the other hand, the anode and cathode layers of an SOFC are most effective with high porosities, of approximately 30–40 vol.%, to allow for adequate gas diffusion. In this article, we address the challenge of creating a high level of porosity in a plasma-sprayed nickel/yttria-stabilized zirconia (Ni/YSZ) anode coating for an SOFC.

There are three previously reported methods to introduce added porosity to a plasma-sprayed Ni–YSZ anode. A popular approach is to start with nickel oxide (NiO) powder rather than pure nickel. The plasma-sprayed coating is therefore composed of NiO–YSZ, and a post-spray reduction step must be used to convert the inactive NiO to the electrocatalytic Ni. NiO has a lower density ($\rho_{NiO} = 6.67\,g\,cm^{-3}$) than Ni ($\rho_{Ni} = 8.9\,g\,cm^{-3}$), so with the reduction comes a volume change and the creation of porosity.

To ensure good electrical conductivity throughout the anode, the amount of Ni phase in the reduced coating should be above the upper percolation threshold of approximately 30 vol.% of the solid phases [1]. To achieve 35–50 vol.% Ni in the solid phases after reduction, one would require a starting NiO–YSZ powder composition of 50–65 wt% NiO. Upon complete reduction of NiO to Ni, this starting powder composition range will theoretically create 19–26 vol.% porosity. However, in practice, some of the NiO may remain unreduced if surrounded entirely by YSZ, and generally, there will be some sintering and coalescing of the Ni particles, so that the actual porosity gained by reduction will be less than the theoretical value.

* Corresponding author. Tel.: +1 416 978 3835; fax: +1 416 978 7753.
E-mail address: kesler@mie.utoronto.ca (O. Kesler).

0378-7753/$ – see front matter © 2012 Elsevier B.V. All rights reserved.
doi:10.1016/j.jpowsour.2012.02.046

The second method to introduce porosity in a plasma-sprayed coating is to adjust the spray parameters to produce a more porous microstructure, regardless of the type of feedstock used. This usually requires having partially melted particles, as opposed to fully melted particles, in the plasma. The partially melted particles retain some of their structure upon impact and aid in creating porosity. The amount of porosity created generally increases with less melting; however, the deposition efficiency and cohesion of the coating can drop significantly as the particles become less molten in the plasma.

The third method to introduce porosity in a Ni–YSZ anode is by using pore formers. Pore formers are solid particles, typically organic, that are present during the formation of the coating, but volatilized during a post-production thermal cycle, leaving behind a porous microstructure. Pore formers – including starch [2–4], graphite [2,3,5,6], carbon [3,7,8], polyethylene [2], flour [7], and saccharose [9] – are commonly used in wet ceramic processing to introduce porosity. The use of pore formers in wet ceramic processing can be particularly helpful for anode-supported SOFCs, where the anode is relatively thick and gas transport through the anode layer can significantly affect performance. However, pore formers are not typically used with plasma spray processing, and only a few studies have documented their use [10–12]. Tai and Lessing [10] were able to create a strontium-doped lanthanum manganite (LSM) cathode coating with approximately 40% porosity using a broad LSM particle size distribution (53–180 μm) with 15 wt% solid "Carbospheres" (117–140 μm). Tai and Lessing also used hollow Carbospheres (50–150 μm) and a fine carbon black powder as pore formers. The hollow Carbospheres were not as effective as the solid Carbospheres for producing porosity, and the carbon black could not be homogeneously mixed with the large LSM particles, resulting in low deposition rates [10]. In all cases, the addition of more than 20 wt% carbon pore former resulted in a carbon surface coating on top of a fully dense cathode coating [10]. Fine carbon black (<10 μm) was also used by Kwon et al. [11] to create additional porosity in a NiO/YSZ cermet anode coating. In this case, Kwon et al. [11] used a Ni-coated graphite powder (50 μm) and 8-YSZ (>75 μm) as the anode feedstock and 40 vol.% carbon black to obtain 38% porosity, following a 4-h 800 °C oxidation cycle in air and a 4-h 800 °C reduction cycle in H_2. Without the carbon black, a porosity of approximately 25% was generated using the Ni-coated graphite powder and YSZ feedstock (50:50 vol.%) after subsequent reduction of NiO to Ni [11]. Weckmann et al. [12] also sprayed Ni-coated graphite and YSZ feedstock powder (50:50 wt%) and found that the Ni–graphite/YSZ coating had higher porosity, and cells with anodes produced in that manner had a higher open-circuit voltage (OCV) and lower resistance, but stronger OCV degradation, than those with a sprayed NiO/YSZ coating. It should be noted that although both Kwon et al. [11] and Weckmann et al. [12] used Ni-coated graphite powder, Kwon et al. observed distinct regions of graphite in the as-sprayed coating, while Weckmann et al. saw only traces of remaining carbon. It is likely that the different plasma torches and different spray conditions caused different amounts of carbon deposition in the as-sprayed coatings.

With pore formers responsible for creating porosity in a plasma-sprayed coating, the ceramic particles can be deposited with a higher degree of melting, with the potential for a higher deposition efficiency and better adhesion than in coatings that rely only on partial melting to incorporate porosity. The use of pore formers may also provide more control over the size and shape of the created porosity. The use of pore formers may make it easier to fabricate plasma-sprayed graded-microstructure coatings. The purpose of this study is to investigate the feasibility of using various pore formers in a plasma-sprayed Ni-based anode coating based on the quantity and morphology of the porosity generated in the coating microstructure.

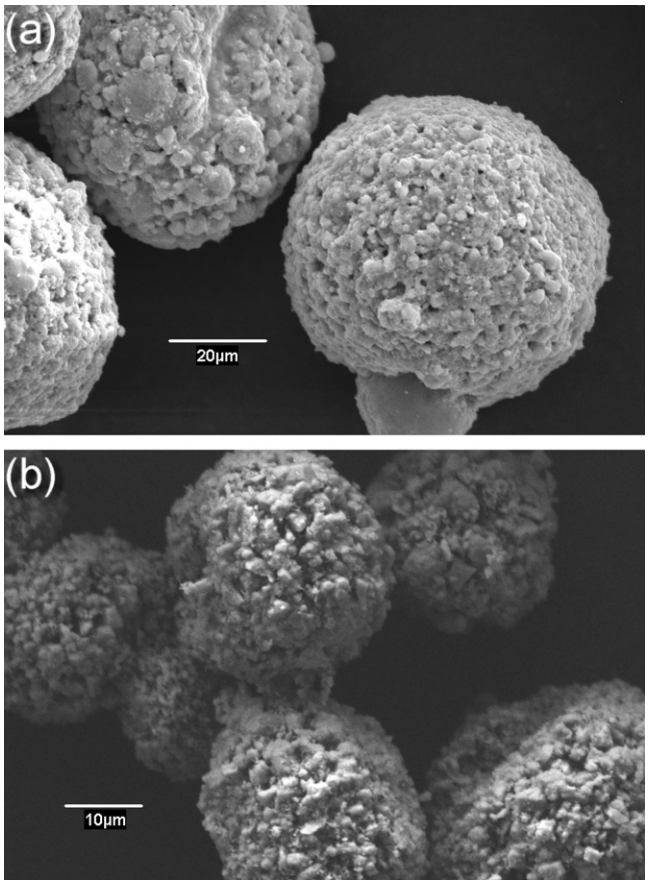

Fig. 1. SEM images of the NiO–YSZ nano-agglomerated powders (a) as-received, and (b) after calcining at 1200 °C for 2 h.

2. Experimental procedure

2.1. Powders

2.1.1. Anode feedstock

To produce SOFC anode coatings, an agglomerated powder of nickel (II) oxide (NiO) and 8 mol% yttria stabilized zirconia (YSZ) nano-particles (Inframat Advanced Materials, Farmington, CT, USA) was used. Nano-sized NiO and YSZ primary particles were chosen to help in the production of a finely structured, homogeneous distribution of NiO and YSZ to enhance the density of active triple-phase boundaries, while the agglomeration of powder into micron-sized spray dried particles is necessary to enable dry powder delivery to the plasma torch. The composition of the NiO–YSZ agglomerates was 70 wt% NiO and 30 wt% YSZ. This composition should theoretically produce 56 vol.% Ni in the solid phases and 28 vol.% porosity after complete reduction of NiO to Ni. The 56 vol.% Ni is well above the percolation threshold, thus ensuring good electronic conductivity.

The as-received NiO–YSZ nano-agglomerated powder (Fig. 1a) was spherical and flowed very well, but was susceptible to breaking up in the powder feed hopper. The NiO–YSZ nano-agglomerated powder was therefore calcined at 1200 °C for 2 h in zirconia crucibles instead of alumina to avoid the formation of $NiAl_2O_4$ spinel. Calcining made the NiO–YSZ powder particles more robust to the agitation of the powder feeder. SEM images (Hitachi-3500) of the calcined NiO–YSZ powder (Fig. 1b) show coarsening of the crystallites on the surface but otherwise an intact structure of the agglomerated particles. X-ray diffraction (XRD) analysis of the as-received and calcined powders confirmed that only the NiO and YSZ phases were present both before and after calcining. However,

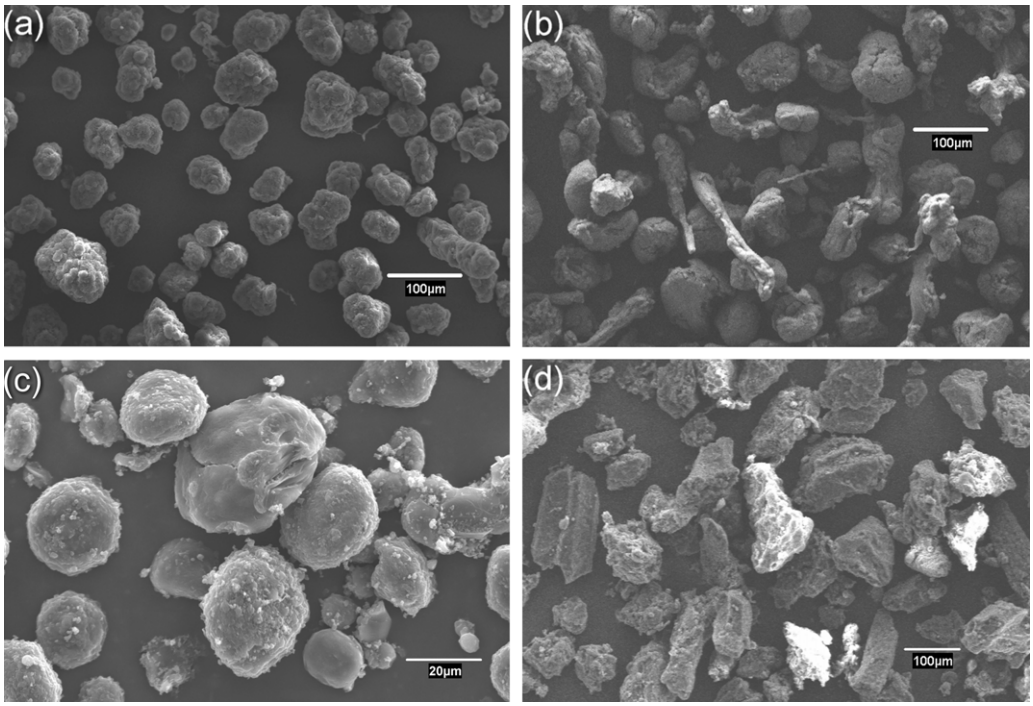

Fig. 2. SEM images of the pore former powders. (a) High density polyethylene, as-received; (b) PEEK, sieved −75 + 45 μm; (c) Osaka Mesocarbon Microbeads (MCMB), grade 25–28, as-received; (d) Robin Hood flour, sieved −106 + 75 μm.

during calcination at 1200 °C, there was significant grain growth, as evidenced by narrowing of the XRD peaks after calcination. The calcined NiO–YSZ powder was then sieved into different size ranges (Table 1).

2.1.2. Pore former powders

Four pore former powders were studied – high-density polyethylene (HDPE), polyether ether-ketone (PEEK), mesocarbon microbead (MCMB) carbon powder, and baking flour.

The HDPE powder particles (Fig. 2a) appeared as round agglomerates with a relatively narrow size distribution. The powder was sieved into different size fractions (Table 1). The as-received PEEK particles showed a significant fraction of long particles with high aspect ratios. Sieving removed most of the long thin particles, although some still remained (Fig. 2b). Mesocarbon microbeads (MCMB), grade 25–28, are a pure carbon powder produced by Osaka Gas Chemicals, Japan. The MCMB carbon powder consisted of primarily spherical particles ranging in size from several microns to 50 μm (Fig. 2c). The carbon powder was sieved to remove the very fine particles that could clog the powder feeder (Table 1).

The commercially available baking flour (Robin Hood All-purpose Flour, Smuckers Foods of Canada, Markham, ON, Canada) contained 71 wt% starch (carbohydrates), 12 wt% gluten (protein), and 16 wt% water, according to the nutritional content label. The as-received flour consisted of mostly angular particles with an aspect ratio of approximately two or less, but with large variations in the size from several microns up to 200 μm. The flour was sieved to reduce size variations and improve flowability. The majority of the flour fell in the −106 + 75 size range (Fig. 2d). All powders were stored in a drying oven at 100 °C to minimize the moisture content during powder processing and plasma spraying.

Removal of the embedded pore former from the plasma sprayed coating is crucial for the purpose of creating porosity. To help determine the necessary heat treatment to burn out the various pore formers, thermo-gravimetric analysis (TGA) was performed on all of the pore former powders. TGA was performed using a Linseis L81/1750 Thermogravimetric Analyzer (Germany). Samples of the pore former powders (~22 mg) were heated at 10 °C per minute up to 1000 °C, then held at 1000 °C for 2 h before cooling, all in still air.

2.1.3. NiO–YSZ–pore former mixtures

The calcined and sieved NiO–YSZ agglomerated feedstock and various pore formers were dry mixed on a jar roller for at least 1 h. To evaluate the performance of the different pore formers, the

Table 1
Properties of the NiO–YSZ and pore former powders. Powder size fractions used are marked with an asterisk.

		NiO–YSZ	HDPE	PEEK	MCMB	Flour
Chemical composition		81 mol% NiO 19 mol% YSZ	—[CH_2—CH_2]$_n$—	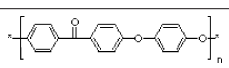	C	$(C_6H_{10}O_5)_n$ $n \sim 100$
Density (g cm^{-3})		6.5	0.96	1.32	2.2	0.77
Melting temperature (°C)		NiO – 1955 YSZ – 2700	143	340	3400	
Sieving mass fractions (%)	−25 μm	18.7			15	
	−32 + 25 μm	19.9			85*	
	−45 + 32 μm	31.1*	1	11.9	Trace	7
	−75 + 45 μm	30.3	48.1*	23.1*		23
	−106 + 75 μm	Trace	50.9	40.6		57*
	+106 μm		<1	24.5		13

pore former to NiO–YSZ ratio in the powder mixture was fixed at 40 vol.%. This value is comparable to the 40 vol.% carbon pore former used by Kwon et al. [11] and the 32 vol.% graphite used by Weckmann et al. [12] for creating Ni–YSZ anode coatings, and was intentionally chosen to be higher than stoichiometrically necessary in order to allow for the volatilization of some of the pore former during the fabrication process.

2.2. Substrates

The anode coatings were plasma sprayed on porous 430 ferritic stainless steel (SS) discs. The SS discs were nominally 25.4 mm in diameter and 1.6 mm thick. Two porosity grades were investigated – media grades (MG) 2 and 0.2 (Mott Corporation, Farmington, CT, USA). The media grade ratings indicate the minimum particle size (in micrometers) that can be trapped by the porous substrates in a filtering application. A study of the Mott media grades by Rose et al. [13] identified MG2 as having the best combination of high total porosity and low surface roughness for metal supported SOFCs. Although the Mott MG0.2 was deemed unacceptable for SOFC use due to closing of the pores after oxidation at 800 °C [13], the MG0.2 substrates exhibited the lowest surface roughness and allowed anode coatings to be fabricated free of pinholes, thus allowing the contributions of the pore formers to the gas permeation rates through the coatings to be more accurately quantified.

2.3. Plasma spraying

2.3.1. Powder delivery

The NiO–YSZ agglomerated feedstock and various NiO–YSZ pore former mixtures were delivered to the plasma torch using a Thermico CPF-2HP powder feeder. For this feeder, the powder feed rate is primarily controlled by the rotation speed of the feed disk. Using a plastic powder collection bottle fitted with particle filters, and computer interfaced to a Denver Instruments SI-6201 precision balance, the gravimetric powder feed rates were measured at various feed disk rotation speeds for each powder mixture. The required feed disk rotation speed for a given feed rate could then be interpolated from the powder feed calibration curves. For each coating, the feed rate of the NiO–YSZ agglomerate powder was kept constant at 25 g min^{-1}. Thus, for a powder mixture of 80 wt% NiO–YSZ agglomerate and 20 wt% pore former, the required feed rate of the 80:20 mixture would be 31.25 g min^{-1}.

2.3.2. Plasma spray torch

The anode coatings were deposited using a Northwest Mettech Axial III torch (North Vancouver, BC, Canada). The Axial III atmospheric plasma spray torch is a 3-anode/3-cathode DC torch that allows the powders to be injected axially. The three plasma streams converge through a single nozzle and the powder is injected at the convergence point. The torch settings were the same for each coating: 250 slpm total plasma gas flow, 76.7% N_2, 23.3% Ar gas composition, 183 A/cathode arc current. From one run to the next, the total torch power varied over a range from 93.1 to 101.4 kW, depending in part on solid loading to the plasma.

The Axial III torch was rastered vertically using an X–Y robot, and the substrates were mounted on a drum rotating at 400 rpm (Fig. 3). The torch and drum were aligned horizontally such that the spray direction and drum surface were nominally perpendicular. The spray distance was set at 100 mm. A total of 80 vertical passes was used to deposit each coating, with each vertical pass traversing 127 mm in 1.4 s. A type K thermocouple probe recorded the temperature on the backside of the substrates and the substrates were pre-heated by just the plasma gases to 300 °C prior to the start of powder delivery. Temperature profiles of a typical spray run are shown in Fig. 4. These profiles were independent

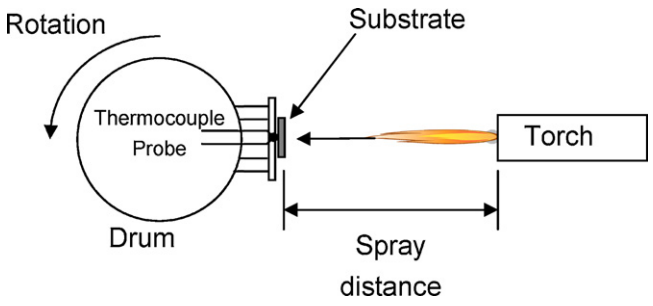

Fig. 3. Plasma spray set-up, top view.

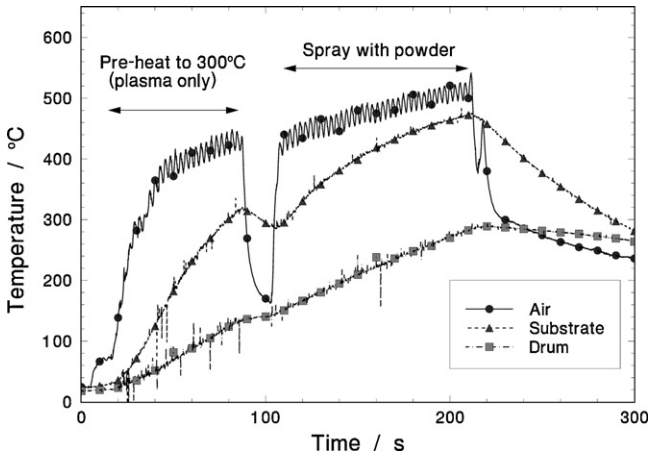

Fig. 4. Temperature profiles at various locations during a typical plasma spray run. The air probe is located 5 mm above the surface of the drum and is protected from direct exposure to the plasma by the substrate holder. The fine oscillations observed with the air probe data are due to the vertical rastering motion of the torch. Symbols are shown for one out of every 100 data points.

of the type of pore former used. Substrate temperatures reached 467 °C ± 8 °C. Typically, eight substrates were mounted and sprayed simultaneously.

2.4. Post-spray heat treatments

The plasma sprayed coatings were then subjected to oxidative and reducing heat treatments. According to the TGA tests on the pore formers (Fig. 5), heating the coatings to 800 °C in air for 2 h

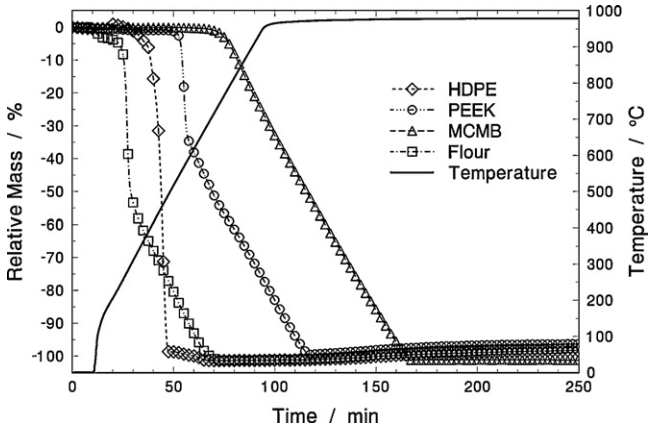

Fig. 5. TGA analysis of the pore former powders heated at 10 °C per minute up to 1000 °C in still air, for Osaka Mesocarbon Microbeads (MCMB), grade 25–28; Robin Hood flour; High density polyethylene (HDPE); and Polyether ether ketone (PEEK). Note that to simplify the plots, only one in twenty data points are represented by the symbols.

should be sufficient to completely remove the pore formers from the coatings, provided that the oxidizing gas has access to the organic phase. Previous experience with reducing NiO–YSZ anode layers found that 2 h at 800 °C in a 20% hydrogen atmosphere (80% nitrogen) was sufficient to reduce the nickel oxide to nickel in the anode layer. In both oxidation and reduction, a temperature of 800 °C was chosen to be representative of the maximum operating temperature of such a metal-supported SOFC.

2.5. Porosity evaluation

The effectiveness of the pore formers in creating porosity was evaluated by two methods – gas flow measurements and porosity image analysis. High purity (99.995%) helium gas from a regulated high-pressure bottle was fed through an Alicat Scientific (Tucson, AZ, USA) dual-valve pressure controller and a specified pressure was delivered to each sample through polyurethane 1.58 mm ID tubes. The sample was held in a specially designed jig that seals around the porous substrate and accommodates samples of various thicknesses. Gas flow was directed in through the coating and out through the porous metal substrate. A 500 sccm Alicat Scientific mass flow meter downstream of the sample and open to atmosphere at the exit measured the gas flow rate through the sample. To account for the effects of the porous substrates on the gas flow, blank substrates without coatings were also tested. The permeability of the coating was then calculated from the gas flow data and the coating thickness. Coating thicknesses were determined by SEM (S3500N, Hitachi, Japan) images of polished coating cross-sections. These measurements did not include surface anomalies, such as thinned areas or surface clumps.

For porosity image analysis, a different set of SEM images of the polished cross-sections was used. Sixteen images were taken for each coating, always central to the coating thickness, at 0.50 mm intervals along the length of the coating. The images were taken at either 3500× or 6000× magnification, depending on the thickness of the coating, with corresponding analysis areas of $35.4 \times 21.2\ \mu m^2$ and $20.0 \times 12.0\ \mu m^2$, respectively. To facilitate the porosity image analysis software in distinguishing between pore and solid, image brightness was reduced and contrast increased to create predominantly black and white SEM images with minimal areas of gray. Use of a lower energy (5 kV) analysis beam further enhanced the contrast between pore and solid by decreasing the depth of field. The image analysis routine was developed within the Clemex Vision PE 5.0 image analysis software (Clemex Technologies, QC, Canada).

3. Results and discussion

3.1. TGA

The results of the TGA procedure on each pore former powder are shown in Fig. 5. In each trial, approximately the same amount of material was tested, ~22 mg, so the slopes of the mass loss curves for the different pore formers may be compared directly. There appear to be two distinct types of loss mechanisms. Rapid mass loss (~2.4–4.3 mg min^{-1}) was only observed with the hydrogen-containing polymer-based pore formers (flour, HDPE, and PEEK). This rapid mass loss is attributed to polymer degradation accompanied by the production and release of volatile phases. These results are consistent with the TGA study of starch by Aggarwal et al. [14], in which non-oxidative degradation resulted in rapid initial mass loss during TGA. The MCMB carbon pore former is not a hydrogen-containing polymer, and therefore did not exhibit polymer degradation.

A slower mass loss (~0.25 mg min^{-1}) was observed as the only mechanism for MCMB removal and as a secondary mass loss mechanism for the PEEK and flour pore formers. Mass loss of the MCMB carbon powder is associated with combustion in the air atmosphere. The slower mass loss rates for the PEEK and flour powders were nearly identical to that of the MCMB, suggesting the same mechanism for mass loss, namely, combustion of carbon. This observation is consistent with TGA results for starch (the main component in flour), in which solid carbonaceous residue produced during initial polymer degradation was consumed via oxidation in an air atmosphere [14]. This slower mass loss mechanism was not observed in the TGA results for HDPE because thermal degradation of HDPE in air leads to the formation of alcohols, ketones, and low-molecular-weight products [15], all of which are volatile at elevated temperatures, with no stable solid residue for subsequent combustion.

The temperatures for the onset of mass loss (defined here by a local minimum in the concavity of the TGA curves) vary from a minimum of 250 °C for the flour pore former to 760 °C for the MCMB carbon powder. The removal of MCMB required the highest temperature heat treatment, and therefore determined the temperature and duration of the oxidation cycle for pore former removal chosen for each coating. A TGA trial with the MCMB powder heated to and held at 800 °C yielded results identical to those in the 1000 °C trial; therefore, a heat treatment to 800 °C for 2 h was deemed sufficient for complete removal of the pore formers from the plasma sprayed coating.

Based on the TGA mass loss data, one can calculate rough estimates of the upper bounds on the lifetimes of the pore former particles, both in-flight and on the substrate surface. An Oseir SprayWatch 2i Portable system (Finland) was used to measure particle temperatures and particle speeds in-flight. For the plasma spray settings used in this study, NiO–YSZ particle speeds of 160 m s^{-1} and particle temperatures of 2000 °C were measured. With this average particle speed and the 100 mm stand-off distance used for spraying, a lower bound on the in-flight mass loss was estimated assuming rates of mass loss similar to those determined by the TGA data. Given the high temperatures during spraying, the actual rate of mass loss in-flight is likely to be much higher than the TGA results would predict, so these estimates should be viewed as the minimum mass loss during plasma spray. Further mass loss may occur after impacting the substrate if the substrate temperature is higher than the temperature required for the onset of mass loss. For the PEEK and flour pore formers, the fraction of mass loss by polymer degradation and by combustion was taken from the TGA data. Calculated estimates of minimum pore former mass loss during plasma spraying are given in Table 2.

It is estimated that a 60 μm HDPE particle would be completely consumed within 8 ms of impacting the substrate. Any HDPE particle smaller than 45 μm would be consumed in-flight and any HDPE particle smaller than 133 μm would be consumed within one rotation of the substrate drum. Given that these estimates represent the best scenario for the survival of HDPE, it is unlikely that the HDPE pore former will survive the plasma spray process and contribute to the plasma sprayed coatings.

The temperatures required for the onset of mass loss of the PEEK and MCMB pore formers, 540 °C and 760 °C, respectively, were higher than the substrate temperature (480 °C), so mass loss of these pore formers would only occur in-flight. Based strictly on the mass loss estimates, one would expect the MCMB and PEEK particle sizes in the plasma sprayed coatings to be comparable to the original particle sizes. However, the size of the pore formers in the coating may still vary if the pore former breaks up or forms a splat upon impact.

The calculated mass loss estimates for a nominal 90 μm flour particle show that most of the flour would survive the in-flight portion if the rates of volatilization are comparable in the plasma and in the TGA, but any flour that survives the plasma would be

Table 2
Parameters and results of mass loss estimates during plasma spray.

	HDPE	PEEK	MCMB	Flour
Temperature for onset of mass loss, T_{ML} (°C)	395	540	760	250
TGA mass loss rates (mg min^{-1})	4.32	2.42 0.24	0.25	3.88 0.30
Mass loss mechanisms	100% decomposition	35% decomposition 65% oxidation	100% oxidation	49% decomposition 51% oxidation
Starting size of powder particle	60 μm (0.11 μg)	60 μm (0.15 μg)	25 μm (0.018 μg)	90 μm (0.29 μg)
Mass loss in-flight	0.045 μg	0.025 μg	0.003 μg	0.040 μg
Mass loss during one drum rotation	11 μg	0* (T_{drum} below T_{ML})	0* (T_{drum} below T_{ML})	0.74 μg

consumed within one rotation of the substrate drum. However, it is still possible for flour particles to contribute to the porosity of the coating if the flour particles that adhere to the substrate interfere with the dense layering of ceramic splats, thus enhancing the porosity between the ceramic particles, and by better dispersing the YSZ within the coating, slowing the rate of nickel sintering after reduction of NiO to Ni.

3.2. Plasma sprayed coatings

3.2.1. Reduction of NiO during plasma spraying

The change in appearance from a green NiO–YSZ nano-agglomerate powder to a black plasma sprayed coating was indicative of an oxidation state change and/or chemical reaction occurring during plasma spraying. To ascertain the possible causes for the physical change due to plasma spraying, X-ray diffraction (XRD) analysis (D8 Advance, Brucker, Germany) was performed on the starting calcined NiO–YSZ powder and on the sprayed coating (Fig. 6). The XRD spectrum for the calcined NiO–YSZ nano-agglomerate powder (Fig. 6a) showed clearly defined peaks representing 8 mol%-YSZ and stoichiometric NiO, as expected. The peak broadening and slight shifts observed in plasma sprayed coatings relative to the XRD peaks of the calcined powder are likely due to a combination of residual stresses and grain refinement during the rapid solidification of the molten droplets during coating formation.

The process of plasma spraying produced two new peaks at $2\theta = 44.5°$ and 51.8° (Fig. 6b) that were not observed with the NiO–YSZ powder. These new peaks were associated with Ni metal. These XRD peaks for nickel have been observed by several plasma spray researchers and have been attributed to NiO reduction during spraying with hydrogen gas [16,17] and from the underlying Ni substrate [18]. In this study, the XRD peaks consistent with the ferritic stainless steel substrate were not detected, indicating that the coating was sufficiently thick to prevent the incoming X-rays from reaching the substrate. Although the plasma gases in this study did not contain hydrogen, but rather only nitrogen and argon, it was clear that NiO reduction occurred during the plasma spray process. Reduction has been observed in plasma sprayed perovskites in high-power plasmas even without hydrogen, suggesting that collisions of energetic plasma ions with the sprayed material were sufficient to cause some reduction of the feedstock during spraying [19]. Partial reduction of stoichiometric NiO to NiO_{1-x} would also explain the change in appearance from a green powder feedstock to a black plasma sprayed coating.

Subsequent oxidation of the plasma sprayed coatings produced another color change from black to green, indicative of re-oxidation of Ni and NiO_{1-x} to stoichiometric NiO. These color change observations, along with further XRD analysis of the coatings after oxidation (Fig. 6c), showed that the oxidation cycle used to burn out the pore formers was sufficient to re-oxidize nearly all the nickel and nickel oxide to stoichiometric NiO, with the amount of metallic Ni barely detectable by XRD after the heat treatment in air. Measurements of the NiO–YSZ coating mass before and after oxidation, with the assumption of full re-oxidation of Ni or NiO_{1-x} to stoichiometric NiO, provided an estimate of the degree of reduction during plasma spraying of 14%. Due to competing mass gain/mass loss processes of Ni oxidation and pore former removal, the same calculations based on mass changes could not be performed on the pore former sprayed coatings. However, using the estimated degree of reduction calculated above, one can calibrate the XRD signals to obtain the relative phase composition of Ni and NiO and derive a value for the degree of NiO reduction to Ni during plasma spraying of NiO–YSZ–pore former powders. With XRD analysis, the quantity of a given phase, X_a, is proportional to the area under any one of its characteristic XRD peaks with Miller index (hkl), $I_{a,hkl}$. Thus, the ratio of Ni to NiO phases in the pore former sprayed coatings can be calculated using

$$\frac{X_{Ni}}{X_{NiO}} = K\frac{I_{Ni,hkl}}{I_{NiO,h'k'l'}},$$

where K is found from correlating the XRD data with the calculated degree of reduction for the NiO–YSZ sprayed coating. Note that it is not necessary to use Ni and NiO XRD peaks with the same Miller indices. The intensities of the strongest XRD signals – (1 1 1) for Ni, and (2 0 0) for NiO – were used.

Fig. 7 shows the results of the XRD analysis on some of the pore former sprayed coatings, focussed on the NiO (2 0 0) and Ni (1 1 1) peaks. The NiO–YSZ coatings sprayed alone and with either flour or PEEK on the Mott media grade 0.2 porous SS substrates all show signs of significant NiO reduction to Ni during the plasma spray process. Using the calculated calibration factor, $K = 0.78 \pm 0.20$, the degree of NiO reduction for the coatings with flour and PEEK pore formers were calculated to be $x_{flour} = 0.18 \pm 0.06$ and $x_{PEEK} = 0.15 \pm 0.05$, respectively. These values agree well with the amount of NiO reduction to Ni that occurs during plasma spraying of the NiO–YSZ powder without pore former. This result implies that the extent of reduction is approximately independent of the addition of pore formers to the powder. XRD analysis of the coatings after reduction (Fig. 6d) showed that the reduction step was sufficient to fully reduce the NiO phase to Ni metal.

3.2.2. Surface morphology

Typical surface morphologies of the plasma-sprayed coatings are shown in Fig. 8. Pinholes through the coating were routinely observed when the media grade 2 (MG 2) substrates were used (Fig. 8a), but pinholes were not observed in the anode coatings deposited on the media grade 0.2 (MG 0.2) substrates (Fig. 8b). The cauliflower-like clumps on the surface were confirmed by energy dispersive X-ray spectroscopy (EDX) to be composed of NiO–YSZ. In all of the coatings, with the exception of the PEEK coating, the

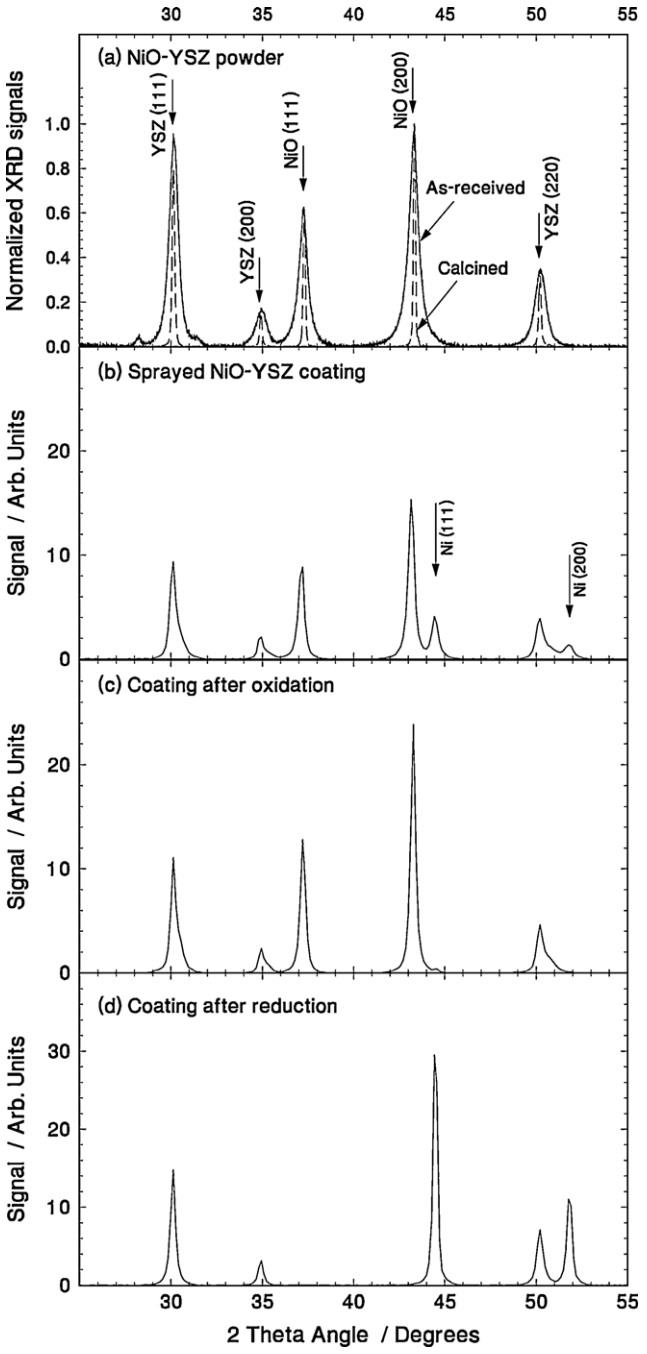

Fig. 6. XRD spectra. (a) XRD spectra for NiO–YSZ nano-agglomerate powder, as-received and calcined at 1200 °C for 2 h (normalized to largest peak). (b) Plasma sprayed NiO–YSZ coating; (c) plasma sprayed NiO–YSZ coating after oxidation; (d) plasma sprayed NiO–YSZ coating after reduction. Peaks were identified using PDF 00-030-1468 for YSZ and PDF 00-047-1049 for NiO.

surface clumps were on the order of the size of the starting NiO–YSZ nano-agglomerate particles. This result suggests that the surface clumps were caused by unmelted or partially melted NiO–YSZ nano-agglomerates.

The surface morphologies for the HDPE and flour coatings were identical to the NiO–YSZ coating, showing no evidence of pore former particles on the surface. These observations are consistent with the mass loss estimates showing that all HDPE and flour on the coating surface would be removed during the plasma spray run.

Both the PEEK and MCMB pore former coatings showed evidence of pore formers on the surface, consistent with the TGA

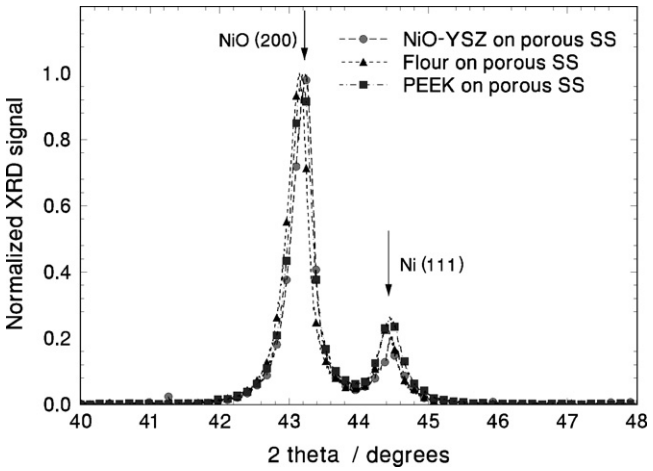

Fig. 7. XRD spectra of the NiO (2 0 0) and Ni (1 1 1) peaks for various NiO–YSZ plasma sprayed coatings, without or with the indicated pore formers.

and substrate temperature data. The PEEK coatings contained surface clumps that were five times larger than the NiO–YSZ nano-agglomerates used in the powder mixture (Fig. 8c). The surface clumps in the PEEK coating were too large to result from unmelted NiO–YSZ particles, so given the significant amount of PEEK in the sprayed coating, it may be more accurate to describe the regions of NiO–YSZ as islands bordered by thin regions of PEEK. PEEK is non-conductive and appears as bright regions in the as-sprayed coating under SEM observation.

Carbon particles on the surface appeared largely intact without significant changes in size or shape (Fig. 8e). The oxidation cycle (800 °C, 2 h in air) was sufficient to remove any carbon remaining on the surface of the coatings, occasionally leaving behind a shell-like structure of NiO–YSZ (Fig. 8f). The oxidative removal of the PEEK pore former from the coating (Fig. 8d) severely degraded the mechanical integrity of the coating. The surface clumps could be easily removed by lightly brushing the surface after oxidation. This degree of mechanical degradation was not surprising, given the significant content of PEEK in the as-sprayed coating and subsequent loss of PEEK material during oxidation.

3.2.3. *Coating microstructure*

The microstructures of the plasma sprayed coatings after spraying, after oxidation, and after reduction were viewed in cross section using SEM. The samples were mounted in epoxy to prevent damage to the thin ceramic coatings during sectioning and polishing. Unfortunately, under SEM or EDX, it is impossible to distinguish between the epoxy filled porosity and carbon based pore formers trapped in the coatings – both were observed as dark regions in the coating. As a result, the microstructures of the as-sprayed and oxidized coatings appeared identical. At first glance, all the as-sprayed coatings (Fig. 9), with the exception of the coating with PEEK pore former, showed similar microstructures consisting of submicron and micron sized dark regions with some linear detachments between splats. Upon close inspection, both the MCMB and flour coatings have a higher density of dark areas than the NiO–YSZ and HDPE coatings. In particular, the flour coatings contain many more of the larger dark regions (Fig. 9e). With the PEEK coating, an abundance of dark areas similar to those in the flour coating could be observed; however, the PEEK coating also appears to be missing large sections of the coating, with only outlined images remaining (Fig. 9c). The outline is due to a layer of NiO–YSZ surrounding the regions of PEEK in the as-sprayed coating. Since the PEEK and epoxy regions appear identical under SEM, the only remaining evidence of the deposited PEEK particles are these outlined areas. It is evident

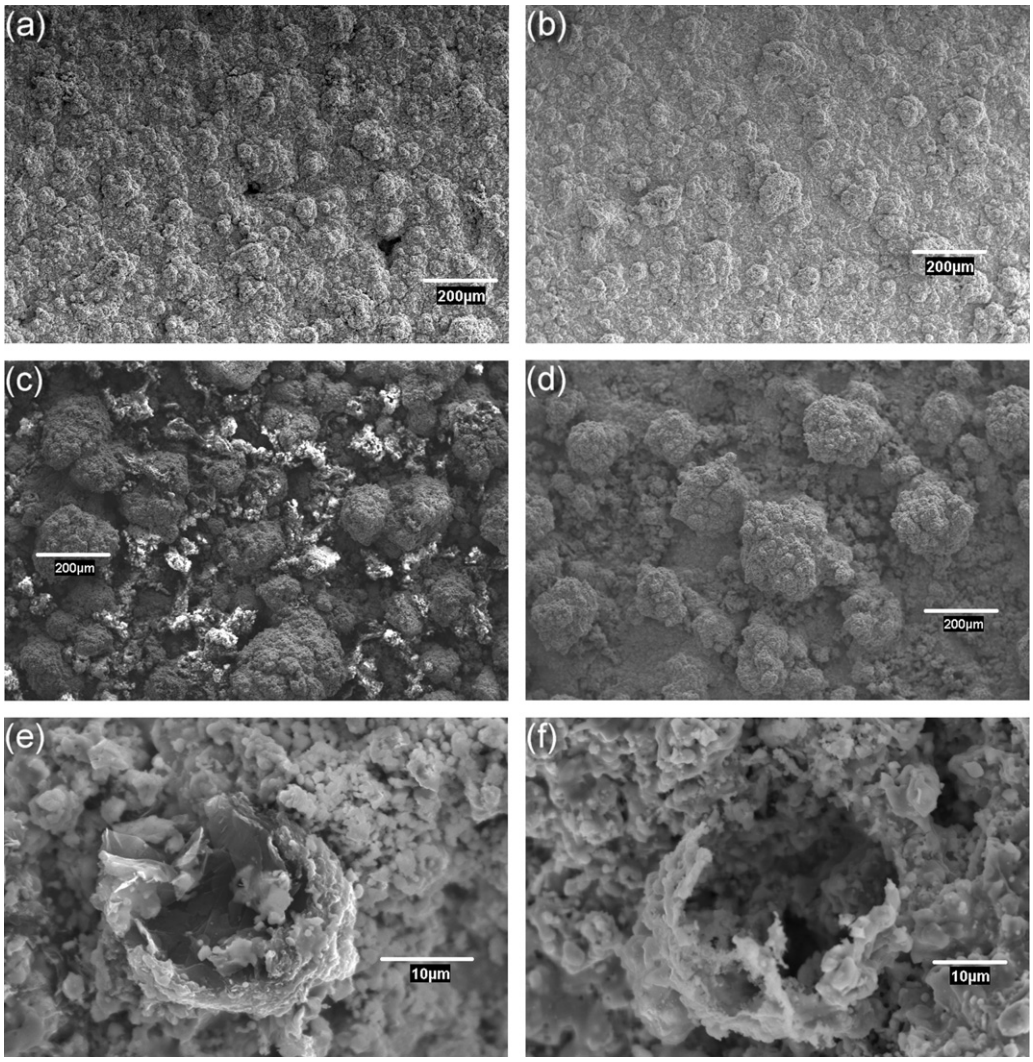

Fig. 8. Surface morphologies of sprayed coatings. (a) Typical coating on MG2 substrate showing pinholes (~30 μm) and surface clumps; (b) typical coating on MG0.2 substrate also with surface clumps but pinhole-free; (c) As-sprayed NiO–YSZ–PEEK coating with bright areas showing locations of PEEK; (d) NiO–YSZ–PEEK coating after oxidation; (e) carbon particle remaining on plasma-sprayed NiO–YSZ–MCMB coating; (f) remaining NiO–YSZ structure after oxidation of NiO–YSZ–MCMB coating.

that removal of such large contiguous sections of PEEK from the coating during oxidation would cause the collapse of any NiO–YSZ supported by the PEEK. The sizes of these regions are consistent with the size fraction of the starting PEEK powder (−75 + 45 μm), as predicted by the in-flight mass loss estimates.

Significant microstructural changes were observed in the coatings following the reduction step (Fig. 10). In the NiO–YSZ coating without pore former, an abundance of linear porosity was observed, primarily running along the length of the coating. The linear porosity could be viewed as channels opening up between successive splats due to the volume reduction associated with the conversion of NiO to Ni metal. The presence of these channels suggests that the NiO and YSZ were deposited as separate layers, rather than as a homogeneous mixture of nano-sized NiO and YSZ particles within splats, as may have been expected when using a NiO–YSZ nano-agglomerated powder. An optical image of the microstructure (Fig. 10b) clearly shows a striated coating structure. To determine the phases corresponding to the different greyscales, an SEM image was taken of the same region under the same magnification and analyzed by EDX. White areas in the coating were found to correspond to pure Ni, dark areas represent YSZ-rich locations, and black spots represent pores. A layered NiO–YSZ microstructure observed by Kwon et al. [10] was attributed to an increased spraying distance that enhanced the accumulation of completely molten NiO or Ni drops in the YSZ framework. With particle temperatures in excess of 2000 °C and the melting temperature of NiO at 1955 °C, the layered structure here may also have been due to completely molten NiO. A layered structure may also have been favored due to the high volume fraction of Ni in the reduced coating. With insufficient YSZ to keep the Ni dispersed, it is also likely that Ni coarsening occurred during the reduction step to promote the layered microstructure.

The reduced HDPE coatings were identical to the reduced NiO–YSZ coating. The reduced MCMB coatings (Fig. 10c) exhibited a greater density of porous features with only an intermittent layered structure compared to the reduced NiO–YSZ coating. The reduced flour coating (Fig. 10d) contained a high density of pore features with a significant number of large pore features (5–10 μm). Very little, if any layered structure was observed with the reduced flour coating. It is believed that the MCMB and flour pore formers were effective in inhibiting the layered NiO–YSZ structure in the sprayed coating by physically interfering with the deposition of the solid layers during coating fabrication. It is possible that gas evolution from oxidative decomposition during spraying also disrupted subsequent layer deposition.

These same SEM cross-section images were also used to determine the coating thickness. It should be noted, however, that the

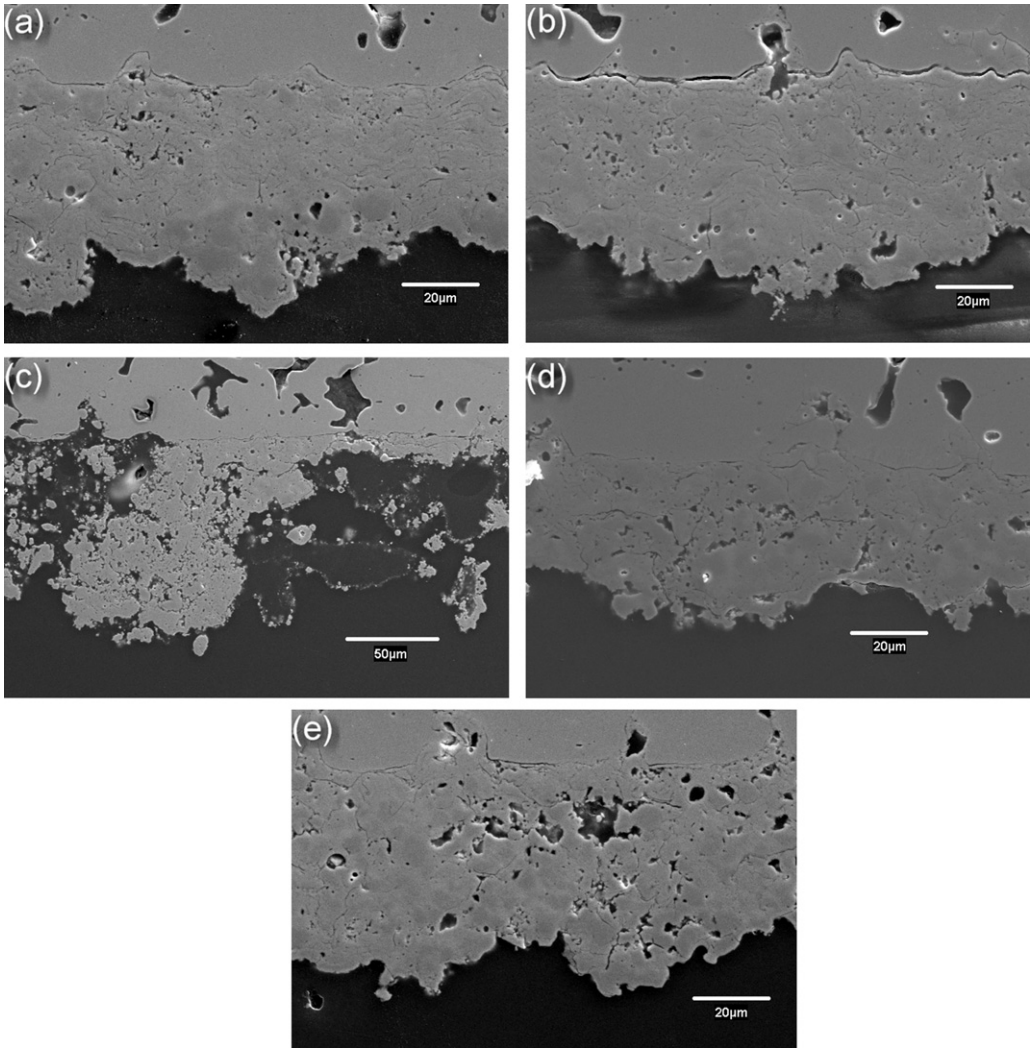

Fig. 9. Cross sectional microstructure of as-sprayed coatings. NiO–YSZ coating (a) without pore formers; (b) with HDPE; (c) with PEEK; (d) with MCMB; (e) with flour.

flour coatings exhibited regions where the coating was very thin (~10 μm), whereas the NiO–YSZ and HDPE coatings did not have any regions below 25 μm in thickness. In one extreme case, the flour coating appears to be only several micrometers thick (Fig. 11). The thickness of the MCMB coating was significantly lower than the average thickness of the other three coating types. The measured coating thicknesses were used for permeability calculations.

3.2.4. Gas flow measurements

The anode coatings were permeation tested in each of their various states – after plasma spraying, after oxidation, and after reduction. A number of substrate blanks – both MG2 and MG0.2 without anode coatings – were exposed to identical thermal cycles to provide references for the gas flow through the substrates only. A sample of the gas flow measurement data is given in Fig. 12. For the coatings sprayed on the MG2 substrate, the NiO–YSZ only coating appears to have higher gas permeation than any of the coatings with pore formers. However, the opposite situation is observed with the coating sprayed on the MG0.2 substrate, where the NiO–YSZ coating had the lowest permeation. This discrepancy in the gas permeation data between the different substrates is due to the presence of pinholes through the MG2 coatings. The number and size of pinholes in the MG2 coatings appear to be the controlling factors for gas flow rates through the MG2 coatings, thus providing the rationale for using the lower surface roughness MG0.2 substrates to prevent the occurrence of pinholes (SEM surface scans of the MG0.2 coatings did not reveal any pinholes). Therefore, only the gas flow data for the anode coatings sprayed on the MG0.2 substrates were analyzed. The slope of the gas flow versus pressure graph provides a measure of the permeation through the coating and substrate.

The permeation through just the coating can be calculated by noting that the gas flow rate is the same through the coating and the substrate, with the total pressure drop across the substrate-coating combination being the sum of the pressure drops across the coating and substrate, with the latter quantity also being directly measured. The pressure drop per unit of gas flow rate is the reciprocal of the gas permeation, P. Since the pressure drops in the coating and substrate are additive, the coating permeation can be determined from the experimentally measured total permeation (substrate and coating) and substrate permeation, as follows:

$$P_{\text{coating}} = \frac{1}{1/P_{\text{total}} - 1/P_{\text{substrate}}}, \quad (1)$$

where P_{total} and $P_{\text{substrate}}$ are the slopes of the gas flow versus pressure graphs for the respective samples.

These calculated coating permeation values are a function of the coating thickness. For comparisons of material properties

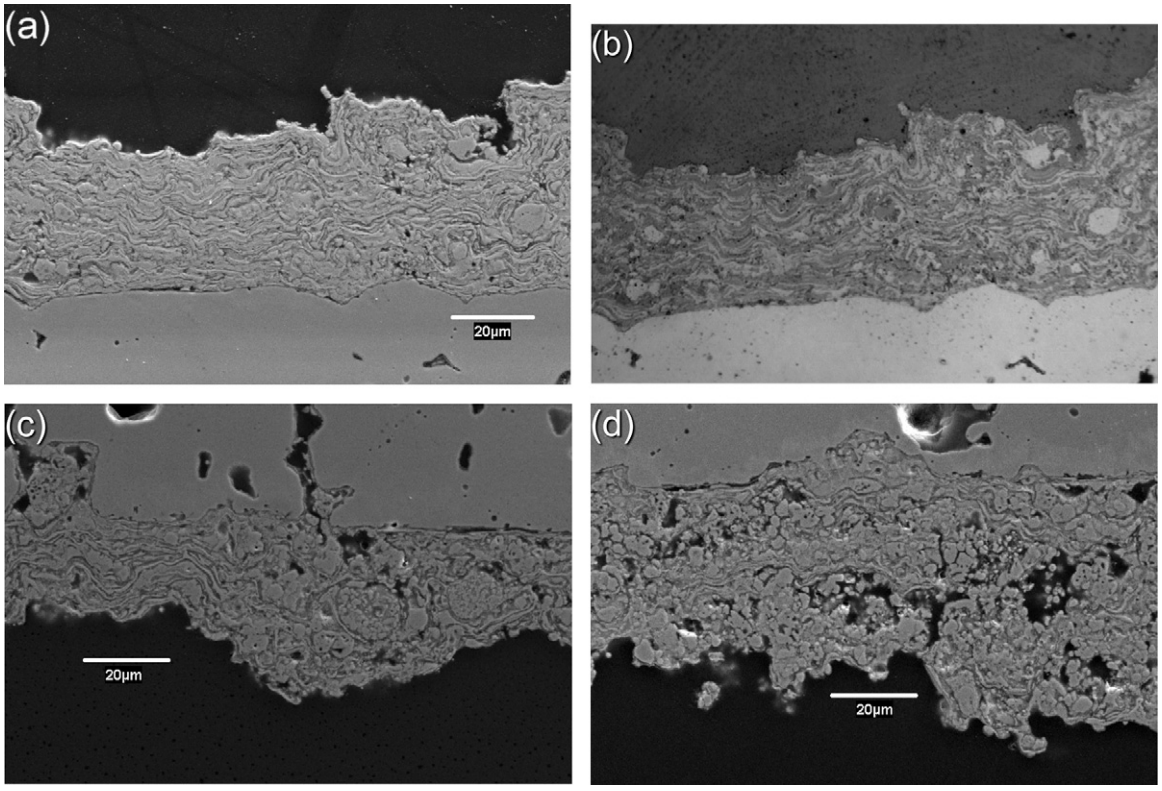

Fig. 10. Cross sectional microstructure of reduced coatings. (a) SEM image of NiO–YSZ coating without pore formers; (b) optical image of NiO–YSZ coating without pore former showing same area as SEM image; (c) SEM image of reduced coating with MCMB pore former; (d) SEM image of reduced coating with flour pore former.

independent of geometry, one can use Darcy's law to calculate the permeability of the anode coatings:

$$Q = \frac{-\kappa A}{\mu}\frac{\Delta P}{L} \rightarrow \kappa_{\text{coating}} = -\frac{\mu L}{A}\frac{Q}{\Delta P} = \frac{\mu L}{A}P_{\text{coating}}, \quad (2)$$

where Q is the gas flow rate ($m^3\,s^{-1}$); κ is the permeability (m^2); A is the cross-sectional area tested (m^2); ΔP is the pressure drop, P_{outlet}–P_{inlet} (Pa); μ is the dynamic viscosity of fluid (Pa s); L is the coating thickness (m).

A summary of the calculated permeability values for the anode coatings deposited on the MG0.2 substrates is shown in Fig. 13. Permeability results for the PEEK-containing coatings are not presented because the mechanical degradation of the coatings made the permeation tests invalid. Weckmann et al. [12] also used permeability measurements to characterize plasma sprayed coatings created with NiO–YSZ and Ni–C–YSZ powders; however, it was not possible to ascertain with certainty the effectiveness of the carbon pore former on permeability in that study, since different plasma torches were used to deposit each powder.

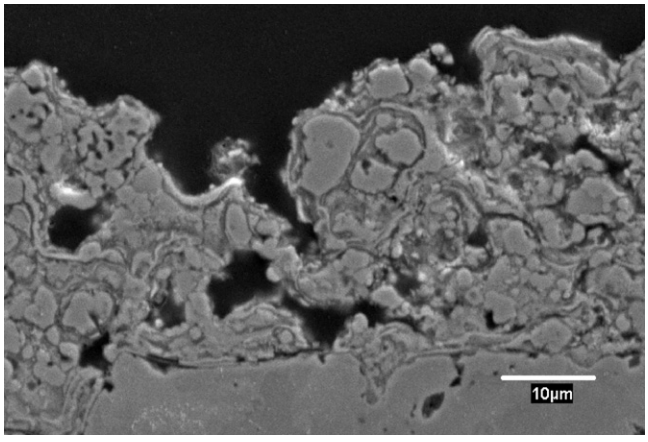

Fig. 11. Polished cross-section of NiO–YSZ–flour coating on MG0.2 substrate after reduction, showing thinned region.

The as-sprayed NiO–YSZ coating exhibited an undesirably low permeability of $3 \times 10^{-17}\,m^2$. After oxidation, permeability of the NiO–YSZ coating decreased further, consistent with oxidation of the Ni formed during spraying to stoichiometric NiO. Upon complete reduction in a hydrogen environment, the final permeability of the Ni–YSZ coating increased to $10^{-16}\,m^2$. A NiO–YSZ coating produced with nano-agglomerated NiO–YSZ feedstock and an APS torch was optimized by Syed and Ilhan [16] to give an as-sprayed coating permeability three orders of magnitude higher than the present results. Syed and Ilhan optimized their coating by creating semi-molten particles – a molten agglomerate surface to ensure good adhesion and a solid interior to preserve the nanostructure and sub-micron porosity [16]. The present NiO–YSZ coatings were not optimized and several factors limited the coating permeability – calcination that coarsened the NiO–YSZ nano-structure, the higher than necessary NiO content (70 wt%), and the use of high power plasma spray conditions likely resulted in more fully molten particles than could be achieved with modified feedstock and process parameters. However, as a preliminary assessment of pore former options, an optimized coating was not required to compare the effectiveness of the various pore formers.

The permeabilities of the as-sprayed, oxidized and reduced HDPE coatings were nearly identical to their NiO–YSZ counterparts. This result is further evidence that the HDPE pore former did not survive the plasma spray process and thus had no effect on the coating properties.

The as-sprayed MCMB coating displayed the same permeability as the NiO–YSZ coating. However, the permeability of the oxidized

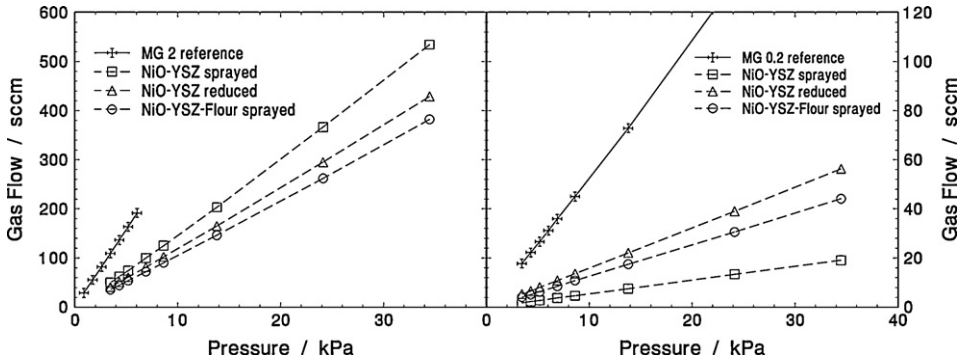

Fig. 12. Permeation data for coatings sprayed on MG2 (left) and MG0.2 (right) substrates. The inlet pressure is measured with respect to the outlet, which is at atmospheric pressure.

MCMB coating was three times higher than that of the oxidized NiO–YSZ coating. This result would appear to suggest that the MCMB formed a portion of the coating, such that the subsequent oxidation cycle removed the carbon and opened new gas pathways, thereby increasing permeability. Subsequent reduction of the MCMB coating led to a further increase in permeability, as expected with the reduction of NiO to Ni

Only the addition of the flour pore former resulted in a significant change in the permeability of the as-sprayed coatings – a five-fold increase to 1.6×10^{-16} m^2 over the NiO–YSZ coatings. It is possible that gas evolution resulting from oxidation of the sprayed flour particles was sufficient to disrupt layering of subsequent deposits, thereby introducing more porosity during spraying and promoting gas transport through the as-sprayed coating. It was noted that a thinned region was observed with the flour coating (Fig. 11) and not with the other coatings. Thus, there exists the possibility that the enhanced as-sprayed permeability was an artifact of thinned regions throughout the flour coating. Permeability of the flour pore former coating increased after oxidation, presumably due to the oxidative removal of some previously trapped flour particles in the coating to leave open gas channels. After the final reduction step, the permeability of the flour coating increased further due to the reduction of NiO to Ni.

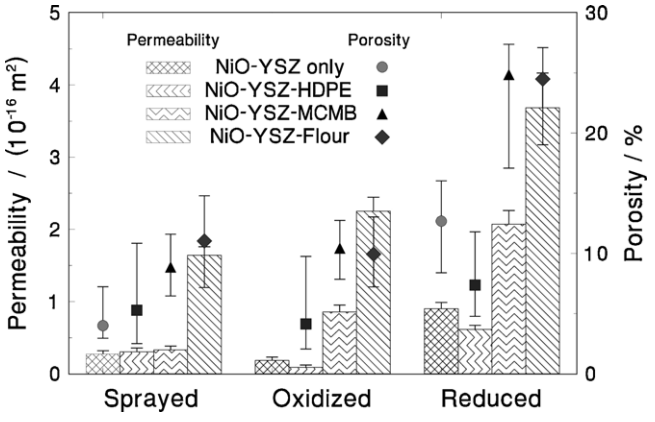

Fig. 13. Calculated permeability values for plasma sprayed anode coatings on MG0.2 substrates during each phase of processing, and porosity values of the NiO–YSZ, MCMB, HDPE, and flour plasma sprayed coatings determined using image analysis. The upper and lower porosity limits are defined in Section 3.2.5. Symbols give the "best" measurement for the actual porosity. Note that the image analyses for the sprayed pore former coatings are calculations of porosity plus residual pore former volume fractions. Image analysis was not performed on the NiO–YSZ coating after oxidation.

3.2.5. Porosity image analysis

An example of one of the images used for porosity image analysis is shown in Fig. 14a. Though largely unsuitable for viewing microstructural details, these high contrast images were ideal for porosity identification. Three porosity levels were measured for each image. A lower porosity limit was determined by setting the greyscale threshold such that the maximum number of porous features could be selected without selecting any solid phase regions (Fig. 14b). This threshold level would underestimate the actual amount of porosity, because the full extents of the porous regions may not be selected and some porous regions may not have been selected at all. The upper porosity limit was determined by setting the greyscale threshold such that the full extents of the gas-phase features were selected (Fig. 14c). This threshold level overestimated the amount of porosity, since solid-phase regions may also be included in this selection. The best porosity estimate entails the use of a greyscale threshold that only selects the porous features without selecting any solid phase regions (criteria for the low porosity limit), and a greyscale threshold that completely selects each porous feature (criteria for the high porosity limit). However, no single greyscale threshold value was able to satisfy both criteria. Instead, both the low and high porosity maps were used to generate the best porosity estimate (Fig. 14d). Porous features were chosen from the high porosity map to ensure that entire features were included, but only those features coincident with the low porosity map were counted, to ensure exclusion of any solid phase features from the best estimate. This filtering process by correlation between the two threshold maps was necessary in order to capture the linear porosity features evident in the microstructures.

The porosity determinations by image analysis of the as-sprayed, oxidized, and reduced coatings are presented in Fig. 13. As previously mentioned, the as-sprayed pore former coating porosity values do not actually represent only the coating porosity, but rather, the volume fraction of porosity plus the pore former phases, due to the inability to distinguish pore former from epoxy-filled porosity in the mounted and polished cross-sections under SEM. From the final porosity determinations after reduction, it was clear that the addition of HDPE had no effect, while additions of MCMB and flour pore formers increase the porosity of the coatings. Mechanical degradation of the PEEK coatings after oxidation did not allow useful porosity measurements.

Porosity image analysis determined that the as-sprayed NiO–YSZ coating without pore former had only 4% porosity, consistent with the low permeability measured for this coating. XRD analysis of the reduced Ni–YSZ coating (Fig. 6d) confirmed complete reduction of the NiO phase to Ni, with the porosity of the reduced Ni–YSZ coating at 13%. This value is much smaller than the theoretical value of 28 vol.% porosity derived from the complete reduction of 70 wt% NiO–30 wt% YSZ. XRD analysis of the

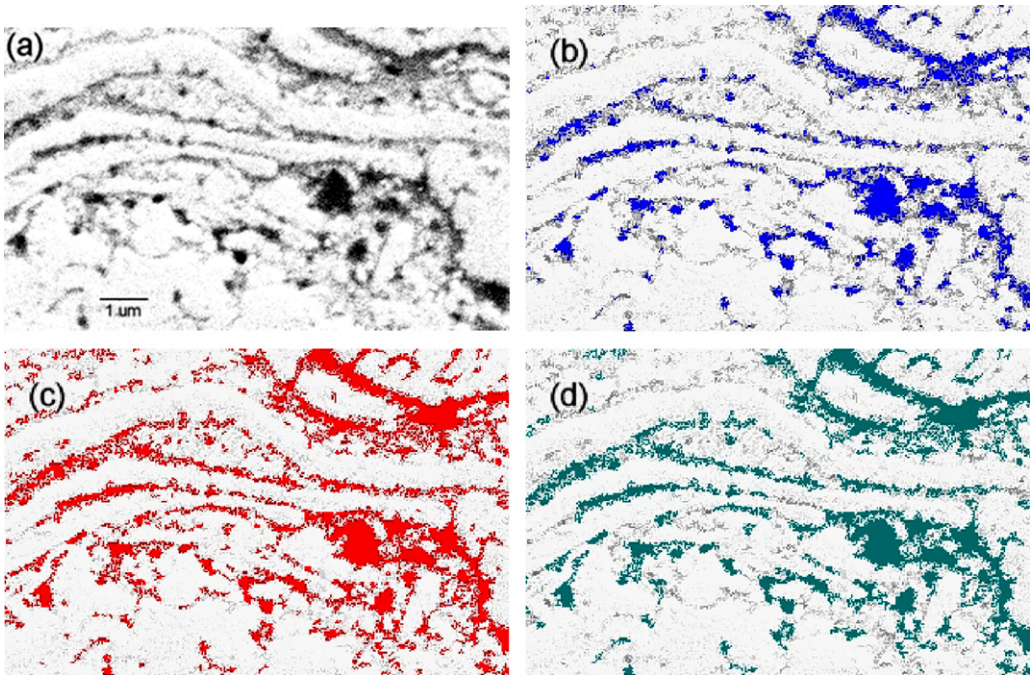

Fig. 14. Images for porosity analysis. (a) Original SEM image; (b) image with gray scale threshold selecting only porosity (no solid regions selected); (c) image with gray scale threshold selecting all porosity but also including some solid regions; (d) best estimate for porosity at which each porous feature is fully defined and no solid regions are selected.

NiO–YSZ coating confirmed that the lower than expected porosity values were not due to incomplete NiO reduction. One possible explanation for the lower porosity values is insufficient YSZ in the agglomerate feedstock powders to form a framework to support and sustain the porosity generated by the NiO to Ni phase change. Without the YSZ framework, some of the open porosity generated by the volumetric reduction from NiO to Ni would collapse due to sintering of the Ni phase. The layering observed in the microstructure was also detrimental to supporting porosity.

The porosity of the HDPE pore former coatings showed no improvement over those of the NiO–YSZ coatings. This result further supports the claim that the HDPE particles volatilize in-flight and do not contribute to the coating. In contrast, the use of MCMB and flour pore formers resulted in significant increases in coating porosity, consistent with the increased permeabilities shown in Fig. 13. The porosities of both the MCMB and flour pore former coatings were similar after oxidation and reduction – ~10% porosity after oxidation and ~24% porosity after reduction. The increase of 14% porosity during reduction was slightly higher than the 9 vol.% increase (from 4 vol.% to 13 vol.%) experienced during reduction of the as-sprayed NiO–YSZ coating. The additional porosity introduced during reduction in the pore former coatings may be associated with the ability of the flour and MCMB pore formers to create a more stable dispersed YSZ framework capable of supporting the porosity created during NiO reduction, by interfering with the formation of densely-stacked splats of the ceramic phases in the coatings during fabrication, as seen in Fig. 10.

3.3. Evaluation of pore formers

3.3.1. HDPE

The addition of 40 vol.% HDPE pore former to a pre-agglomerated NiO–YSZ powder was not effective for increasing the porosity of a plasma sprayed coating. Permeability measurements, porosity image analysis, and SEM observations of the HDPE coating microstructure showed no difference from those of the NiO–YSZ coating. These null results together with the TGA data and mechanics of HDPE degradation have led to the conclusion that all of the HDPE powder is consumed during plasma spraying, either in-flight or quickly volatilized off the substrate. Though HDPE was not a suitable pore former in this study, the ability for HDPE to volatilize in the absence of oxygen is an attractive feature from the point of view of eliminating the need for an intermediate oxidation step for pore former removal (HDPE could be removed simultaneously during NiO reduction). However, this benefit is moot if the HDPE does not survive the coating fabrication process.

3.3.2. PEEK

In the case of the PEEK pore former powder, the plasma sprayed coating contained too much PEEK and upon subsequent oxidative removal, the structural integrity of the coating was compromised. It is believed that the combination of the large particle sizes and the thermal stability of PEEK up to 500 °C allowed the majority of the PEEK particles to survive the plasma and contribute to the coating. Though unsuccessful in the current study, the PEEK powder exhibited several promising characteristics for a plasma sprayed pore former. The PEEK pore former was capable of surviving the plasma in-flight with relatively minor amounts of mass loss due to thermal degradation. The thermal stability of PEEK up to 500 °C during the TGA measurements suggested that PEEK deposited on a substrate with temperatures reaching 470 °C would not be removed during the course of the plasma spray run. Also, given the melting temperature of PEEK (T_m = 343 °C), it was likely that the PEEK particles were fully molten, resulting in good deposition efficiency of the PEEK pore former. While PEEK has the thermal stability to survive the plasma spray process, the required burn-out temperature for its removal is modest. The onset of PEEK mass loss by thermal degradation occurred at 540 °C, so a burn-out temperature of approximately 600 °C should suffice to completely remove PEEK from the coating, compared to the

760 °C needed for the graphitic carbon spheres studied here. A lower burn-out temperature is particularly important for metal-supported cells, in which oxidation of the metal substrate is to be avoided. By using a lower volume fraction and smaller particle size to balance the good deposition efficiency and thermal stability of the PEEK pore former, there is potential for PEEK to be an effective pore former in plasma sprayed coatings.

3.3.3. MCMB

The increased permeability of the MCMB coating after pore former burn-out indicated that connected porosity was generated by the removal of the MCMB phase from the coating. However, the amount of porosity generated was not comparable to the proportion of MCMB in the feedstock. TGA analysis of the MCMB powder showed that MCMB had the highest thermal stability of the pore formers tested, requiring 760 °C for the onset of mass loss, and calculations of mass loss in-flight and surface observations show that the MCMB pore former successfully survived the plasma spray process with little mass loss. Yet, the MCMB particles did not contribute as expected to the coating microstructure. It is believed that the MCMB pore former has low deposition efficiency because by nature, carbon does not melt at atmospheric pressure, but rather sublimates at high temperature (~3600 °C). If the plasma sprayed MCMB particles remained solid, they would not form splats upon impact and would tend to rebound from the substrate, resulting in a low deposition efficiency. Also, if the NiO–YSZ co-deposited powders are not sufficiently molten to cover the carbon particles, the carbon may not become trapped in the coating, and may be more prone to reflect off the substrate [20]. Other researchers using plasma sprayed carbon powders, e.g. Kwon et al. [11] and Weckmann et al. [12], did not report any concerns with the deposition of plasma sprayed Ni-coated graphite particles. It is likely that the Ni coating was fully molten in the plasma, forming a semi-molten particle (molten Ni exterior, solid carbon interior), allowing the carbon to stick to the substrate. A hotter plasma or longer residence time in the plasma to produce fully molten NiO–YSZ may allow a higher relative deposition efficiency for the MCMB, but potentially at a trade-off of lower porosity from partial melting of the ceramic phases.

The increased permeability after oxidation made it clear that at least some of the MCMB pore former must have been present in the coating. SEM observations of the MCMB microstructure (Fig. 9d) did not show any large (~20 μm) carbon particles within the bulk of the coating – it is likely that these large carbon particles simply reflected off the substrate surface. Smaller MCMB fragments could be co-deposited with semi-molten NiO–YSZ and contribute to the porosity of the coating. Given the thermal stability of the carbon during plasma spraying, a strategy to increase the MCMB deposition efficiency is to use much smaller particles, 1–2 μm rather than 25 μm, to increase the likelihood of co-deposition with the other powders. Though the MCMB particles could be successfully removed by oxidation at 800 °C, the high temperature needed to remove graphitic carbon may present restrictions on the type of metal substrates that can be used [13].

The final process of reduction further increased the porosity and permeability values of the MCMB coatings to double those of the NiO–YSZ coatings without pore former. Microstructural observations of the MCMB coating showed a less striated structure compared to the NiO–YSZ coating, suggesting that the presence of the MCMB particles acts to disrupt the layering of NiO–YSZ splats, thereby creating a more stable framework of YSZ that could support the increased porosity generated during NiO reduction.

3.3.4. Flour

Like the MCMB pore former, the flour pore former also suffered from low relative deposition efficiency; however, this result was due to the thermal instability of the flour (as opposed to the thermal stability of MCMB). The TGA data for flour showed that most deposited flour particles exposed to air could completely combust between successive passes of the rotating substrate in front of the torch path. Oxidation of the flour coating slightly increased the permeability of the coating, indicating that some flour did survive the plasma spray process and contribute to the coating. One possible mechanism to allow the survival of the flour phase is a NiO–YSZ splat immediately covering the deposited flour phase, thereby shielding the flour from further oxidation during spraying. However, such a mechanism is unlikely to trap large amounts of flour in the coating, and indeed, only a small change in porosity was observed after oxidation of the as-sprayed coating.

Though the rapid oxidation of flour during plasma spraying may be detrimental to its deposition efficiency, it is possible that the volatile products from oxidation may have contributed to the enhanced permeability of the as-sprayed flour coating (Fig. 13). Tai and Lessing [10] have suggested that gas evolved from carbon oxidation during spraying prevented the formation of dense layers. Like the MCMB powder, the addition of the flour pore former appeared to disrupt the dense layering observed in the NiO–YSZ coatings and helped retain the porosity generated during NiO reduction. Though the measured porosities of the flour and MCMB coatings after reduction were similar, the permeability of the flour coating was twice as large as that of the MCMB coating (and four times larger than that of the NiO–YSZ coating). It appears that the flour was more effective at generating connected porosity through the coating to enhance gas permeability, possibly due to the volatile combustion products of flour creating microchannels through to the surface. However, local thinning of the flour coatings could also have contributed to the higher permeation rates measured, so the carbon and flour pore formers may contribute similarly to anode gas permeation as well as porosity during the plasma spray fabrication process.

4. Conclusions

HDPE, PEEK, MCMB and flour powders were evaluated as possible pore formers for plasma sprayed NiO–YSZ anodes.

The plasma sprayed NiO–YSZ powder with 40 vol.% HDPE produced a coating with microstructure, permeability, and porosity characteristics identical to those of a plasma sprayed NiO–YSZ coating without pore former. These results, combined with the thermal degradation behavior of HDPE, have led to the conclusion that the HDPE powder was completely consumed during the plasma spray process and could not contribute to the plasma sprayed coating. HDPE is therefore not a suitable pore former for plasma sprayed coatings made with similar process conditions as those used in this study.

The deposition efficiency of the PEEK powder was much higher than those of the other pore formers tested, such that addition of 40 vol.% PEEK to the NiO–YSZ powder produced a plasma sprayed coating with a high fraction of the PEEK phase. Upon subsequent oxidative removal of PEEK from the coating, loss of the PEEK phase destroyed the mechanical integrity of the coating, and further analysis could not be performed. The thermal properties of PEEK allowed a good deposition efficiency during plasma spraying and a reasonable temperature for removal by combustion. Though ineffective under the current conditions, PEEK powder displayed promise as a pore former for plasma sprayed coatings, if suitable initial particle sizes and morphologies can be obtained.

Inclusion of 40 vol.% MCMB in the NiO–YSZ powder produced a plasma sprayed coating with twice the porosity and permeability of a NiO–YSZ coating without pore former. The MCMB powder was an effective pore former for plasma spraying; however, it has a low deposition efficiency and requires high oxidation

temperatures for its removal, thus potentially leading to incompatibilities with metal-supported cells.

Under the conditions in this study, flour appeared to be the most effective pore former powder, producing plasma sprayed anode coatings with up to four times greater permeability than a similarly sprayed NiO–YSZ coating without pore former, and double the porosity. The low temperature oxidation behavior of flour led to low relative deposition efficiencies; however, the combustion of flour also released gas during spraying that may have helped to increase the porosity of the coating by interfering with the dense layering of ceramic splats observed in the coatings without pore former. Flour was preferable to MCMB as a pore former due to the higher permeability generated and the lower temperature required for its removal by oxidation.

Acknowledgements

This work was supported by the Natural Sciences and Engineering Research Council of Canada (NSERC). The authors thank Mark Robertson of the Canadian National Research Council Institute for Fuel Cell Innovation (NRC-IFCI) for his training and guidance on the use of the SEM, EDX, XRD, and sample preparation equipment. Also, particular thanks to UBC SOFC group member Lars Rose, for many discussions and for his assistance with the gas permeation and TGA equipment.

References

[1] D.W. Dees, T.D. Claar, T.E. Easler, D.C. Fee, F.C. Mrazek, J. Electrochem. Soc. 134 (9) (1987) 2141–2146.
[2] S.F. Corbin, P.S. Apte, J. Am. Ceram. Soc. 82 (7) (1999) 1693–1701.
[3] A. Sanson, P. Pinasco, E. Roncari, J. Eur. Ceram. Soc. 28 (2008) 1221–1226.
[4] O. Kesler, R.L. Landingham, Solid State Ionics – 2002 Symposium Materials Research Society Symposium Proceedings, vol. 756, 2003, pp. 539–544.
[5] R.M.C. Clemmer, S.F. Corbin, Solid State Ionics 166 (2004) 251–259.
[6] L. Zhang, S.P. Jiang, W. Wang, Y. Zhang, J. Power Sources 170 (2007) 55–60.
[7] J. Hu, Z. Lu, K. Chen, X. Huang, N. Ai, X. Du, C. Fu, J. Wang, W. Su, J. Membrane Sci. 318 (2008) 445–451.
[8] P. Jasinski, T. Suzuki, V. Petrovsky, H.U. Anderson, Electrochem. Solid-State Lett. 8 (4) (2005) A219–A221.
[9] T. Delahaye, O. Joubert, M. Caldes, Y. Piffard, P. Stevens, Solid State Ionics 177 (2006) 2945–2950.
[10] L. Tai, P.A. Lessing, J. Am. Ceram. Soc. 74 (3) (1991) 501–504.
[11] O.C. Kwon, C. Lee, S.Y. Hwang, Conference Proceedings ITSC, 2007.
[12] H. Weckmann, A. Syed, Z. Ilhan, J. Arnold, J. Thermal Spray Tech. 15 (4) (2006) 604–609.
[13] L. Rose, O. Kesler, C. Deces-Petit, T. Troczynski, T. Sobolyeva, R. Maric, Conference Proceedings, HFC Vancouver, 2009.
[14] P. Aggarwal, D. Dollimore, K. Heon, J. Therm. Anal. 50 (1997) 7–17.
[15] Yu Bolbukh, P. Kuzema, V. Tertykh, I. Laguta, J. Thermal Anal. Calorim. 94 (2008) 727–736, 3.
[16] A.A. Syed, Z. Ilhan, Thermal Spray 2007 Proceedings, 2007, pp. 671–676.
[17] T. Grinys, S. Tamulevicius, I. Prosycevas, S. Meskinis, Plasma Process. Polym. 4 (2007) S181.
[18] C. Hwang, C.H. Tsai, C.H. Lo, C.H. Sun, J. Power Sources 180 (2008) 132–142.
[19] J. Harris, O. Kesler, J. Thermal Spray Tech. 19 (1–2) (2010) 328–335.
[20] M. Gui, S.B. Kang, Mater. Lett. 51 (2001) 396–401.